PHYSICAL REVIEW C **76**, 044317 (2007)

Clustering and triaxial deformations of ^{40}Ca

Yasutaka Taniguchi,[1,2] Masaaki Kimura,[3] Yoshiko Kanada-En'yo,[2] and Hisashi Horiuchi[4]
[1]*Department of Physics, Kyoto University, Kyoto 606-8502, Japan*
[2]*Yukawa Institute for Theoretical Physics, Kyoto University, Kyoto 606-8502, Japan*
[3]*Institute of Physics, University of Tsukuba, Tsukuba 305-8571, Japan*
[4]*Research Center of Nuclear Physics, Osaka University, Ibaraki 567-0047, Japan*

(Received 5 July 2007; revised manuscript received 3 September 2007; published 23 October 2007)

We have studied the positive-parity states of ^{40}Ca using antisymmetrized molecular dynamics (AMD) and the generator coordinate method (GCM). Imposing two different kinds of constraints on the variational calculation, we have found various kinds of ^{40}Ca structures such as a deformed-shell structure, as well as α-^{36}Ar and ^{12}C-^{28}Si cluster structures. After the GCM calculation, we obtained a normal-deformed band and a superdeformed band together with their side bands associated with triaxial deformation. The calculated $B(E2)$ values agreed well with empirical data. It was also found that the normal-deformed and superdeformed bands have non-negligible α-^{36}Ar cluster and ^{12}C-^{28}Si cluster components, respectively. This leads to the presence of an α-^{36}Ar higher nodal band occurring above the normal-deformed band.

DOI: 10.1103/PhysRevC.76.044317 PACS number(s): 21.60.−n, 23.20.−g, 27.30.+t, 27.40.+z

I. INTRODUCTION

Nuclear dynamics possess various aspects depending on mass regions, excitation energies, and so on. In light-weight nuclei, it is known that clustering plays a significant role in the features of ground and excited states [1,2]. In contrast, in heavier nuclei, the clustering effects are not clear, though many theoretical [3,4] and experimental [5] studies have been conducted. In the fp-shell region, the focus should be on proton-rich $N \sim Z$ nuclei, because such nuclei can have a clustered structure comprising stable nucleus. Moreover, proton-rich nuclei have a large radius and stronger Coulomb repulsion and may also derive a cluster structure. In the scope of this research, the features of cluster structures in ^{40}Ca are a key issue, because they are the heaviest $N = Z$ stable nuclei, and many experimental data exist for this nuclei. In this paper, we have studied the structure of ^{40}Ca as a starting point to understand the structures of medium- and heavy-weight $N \sim Z$ nuclei. ^{40}Ca has a typical double closed-shell structure nucleus and has a spherical ground state. However, it is known that many kinds of deformed band appear in low-energy regions. The first $K^\pi = 0^+$ band built on the $J^\pi = 0_2^+$ state (3.35 MeV) is considered to be a normal-deformed (ND) state and the dominant configuration is $4p$-$4h$ [6]. The $K^\pi = 2^+$ band built on $J^\pi = 2_2^+$ (5.25 MeV) exists just above the $K^\pi = 0^+$ band. It has been suggested that the ND band deforms triaxially and has the $K^\pi = 2^+$ side band owing to triaxiality [7,8].

The α-^{36}Ar cluster structure has been studied for a long time, because ^{40}Ca is an analog of ^{16}O, which has an α-^{12}C cluster structure in the first $K^\pi = 0^+$ band, as a double closed-shell nuclei. Calculations with the local potential model [9–11] and α-^{36}Ar orthogonal condition model (OCM) [12,13] have been performed theoretically. Ohkubo *et al.* suggested that the first $K^\pi = 0^+$ band (ND) has an α-^{36}Ar structure and predicted that its parity-doublet $K^\pi = 0^-$ band and α-^{36}Ar higher nodal band exist in highly excited states [10]. Sakuda and Ohkubo obtained the $K^\pi = 2^+$ band as well as the $K^\pi = 0^+$ and 0^- states using the α-^{36}Ar OCM and succeeded in reproducing $E2$ transition strengths [13]. Experimentally, the α-^{36}Ar structure is studied through the ^{36}Ar(^{6}Li,d)^{40}Ca reaction [14,15]. The states in these $K^\pi = 0^+$ and 0^- bands are populated by the α-transfer reactions and have large α spectroscopic factors [14]. In the experiments we describe, the α-^{36}Ar higher nodal states were also observed [15].

It has been suggested that the states in the $K^\pi = 0^+$ rotational band built on the $J^\pi = 0_3^+$ state (5.21 MeV) have an $8p$-$8h$ configuration [7], and they have been observed during experimental work searching for the $8p$-$8h$ states with ^{32}S(^{12}C, α)^{40}Ca reactions [16]. Because of the strong population in the multinucleon transfer data and the strong $E2$ transitions [17], the 0^+ (5.21 MeV), 2^+ (5.63 MeV), and 4^+ (6.54 MeV) states have been thought to belong to the superdeformed (SD) band with the dominant $8p$-$8h$ configuration. Recently, by using GAMMASPHERE array detectors, the level structure of the deformed bands in ^{40}Ca has been explored and many excited states up to high spin have been discovered. This band was thus confirmed as the SD band [18].

Motivated by these the experimental observations, many theoretical microscopic studies on deformed states of ^{40}Ca have been performed recently with the methods of Skyrme-Hartree-Fock (SHF) [19], SHF-BCS + GCM [20], spherical-basis antisymmetrized molecular dynamics (AMD) [21], and the shell model [22]. Inakura *et al.* performed cranked SHF calculations without assuming axial symmetry, though energy levels were not calculated [19]. Bender *et al.* performed SHF-BCS + GCM calculations [20]. Although they calculated energy levels and quadrupole transition strengths in the ND and SD bands, they could not study triaxiality nor side bands because they assumed axial symmetry. In these studies, the relationship between deformed states and cluster structure was not discussed. It has been suggested that the SD state forms a ^{12}C-^{28}Si-like cluster structure in spherical-basis AMD [21]. Within the spherical-basis AMD, neither ND nor SD states exhibit triaxiality.

The purpose of the present study is to understand the clustering and triaxial deformations in the low-energy states of ^{40}Ca in a unified manner. We use the framework of AMD + GCM. The basis functions of the generator coordinate method (GCM) are obtained by energy variation after parity projection with constraints. We adopted two kinds of constraints. One is a constraint on the quadrupole deformation parameter β (β constraint) and the other is on the distance d between clusters' centers of mass (d constraint). It has already been proven that the d constraint is useful for obtaining various kinds of clustering wave function, which are not computed within a simple β constraint [23]. For example, the ^{8}Be(2α)-^{12}C cluster structure in ^{20}Ne is calculated with a d constraint but not with the β constraint. Also, in the case of ^{40}Ca, many kinds of cluster structure, for example, α-^{36}Ar, ^{8}Be(2α)-^{32}S, and ^{12}C-^{28}Si, can be calculated with the d constraint, although no cluster structure is obtained in ^{40}Ca with the β constraint. We superposed mean-field-type and cluster-type wave functions calculated with β and d constraints, respectively, and calculated energies and $E2$ transition strength. We analyzed the superposed wave functions to investigate clustering and triaxial deformations.

This paper is organized as follows. In the next section (Sec. II), we explain the framework of this study. The calculated results and discussions are presented in Sec. III, and lastly, we present a summary in Sec. IV.

II. FRAMEWORK

A. Wave function and Hamiltonian

We used the theoretical framework of AMD + GCM. In the present study, the AMD wave function is a Slater determinant of triaxially deformed Gaussian wave packets (deformed-basis AMD),

$$|\Phi_{\rm int}\rangle = \hat{\mathcal{A}}|\varphi_1, \varphi_2, \ldots, \varphi_A\rangle, \tag{1a}$$

$$|\varphi_i\rangle = |\phi_i, \chi_i, \tau_i\rangle, \tag{1b}$$

$$\langle \mathbf{r}|\phi_i\rangle = \prod_{\sigma=x,y,z} \left(\frac{2\nu_\sigma}{\pi}\right)^{\frac{1}{4}} \exp\left[-\nu_\sigma\left(r_\sigma - \frac{Z_{i\sigma}}{\sqrt{\nu_\sigma}}\right)^2\right], \tag{1c}$$

$$|\chi_i\rangle = \alpha_i|\uparrow\rangle + \beta_i|\downarrow\rangle, \tag{1d}$$

$$|\tau_i\rangle = |p\rangle \text{ or } |n\rangle. \tag{1e}$$

Here, the complex parameters $\mathbf{Z}_i$, which represent the centroids of the Gaussian in phase space, take independent values for each single-particle wave function. The width parameters ν_x, ν_y, and ν_z are real parameters and take independent values for each of the x, y, and z directions, but are common for all nucleons. The spin part $|\chi_i\rangle$ is parametrized by α_i and β_i and the isospin part $|\tau_i\rangle$ is fixed as $|p\rangle$ (proton) or $|n\rangle$ (neutron). The quantities ($\mathbf{Z}_i, \alpha_i, \beta_i, \nu_x, \nu_y, \nu_z$) are variational parameters and are optimized by energy variation as explained in the next section.

The trial wave function in the energy variation with constraints is a parity-projected wave function,

$$|\Phi^\pi\rangle = \frac{1 + \pi\hat{P}_r}{2}|\Phi_{\rm int}\rangle, \tag{2}$$

where π is parity and $\hat{P}_r$ is the parity operator. In this study, we will discuss positive-parity states.

The Hamiltonian is

$$\hat{H} = \hat{K} + \hat{V}_N + \hat{V}_C - \hat{K}_G, \tag{3}$$

where $\hat{K}$ and $\hat{K}_G$ are the kinetic energy and the energy of the center-of-mass motion, respectively, and $\hat{V}_N$ is the effective nucleon-nucleon interaction. We have used the Gogny D1S force (D1S) and the Skyrme SLy7 force (SLy7) in the present work. The Coulomb force $\hat{V}_C$ is approximated by a sum of seven Gaussians.

B. Energy variation, angular momentum projection, and the generator coordinate method

We performed energy variation and optimized the variational parameters included in the trial wave function [Eqs. (1)] to find the state that minimizes the energy of the system,

$$E^\pi = \frac{\langle\Phi^\pi|\hat{H}|\Phi^\pi\rangle}{\langle\Phi^\pi|\Phi^\pi\rangle} + V_{\rm cnst}. \tag{4}$$

Here, we add the constraint potential $V_{\rm cnst}$ to the expectation value of Hamiltonian $\hat{H}$ to obtain local minimum energy states under the optional constraint condition. In this study, we employed two types of constraint, which are on the quadrupole deformation parameter β (β constraint) and the distance between clusters' centers of mass d (d constraint) by employing the potential

$$V_{\rm cnst} = \begin{cases} v^\beta_{\rm cnst}(\beta - \tilde{\beta})^2 & \text{for} \quad \beta \text{ constraint}, \\ v^d_{\rm cnst}(d_{{\rm C}_m\text{-}{\rm C}_n} - \tilde{d}_{{\rm C}_m\text{-}{\rm C}_n})^2 & \text{for} \quad d \text{ constraint}. \end{cases} \tag{5}$$

Here β is the matter quadrupole deformation parameter, which is defined in Ref. [24], and $d_{{\rm C}_m\text{-}{\rm C}_n}$ is the distance between the clusters' centers of mass ${\rm C}_m$ and ${\rm C}_n$, that is,

$$d_{{\rm C}_m\text{-}{\rm C}_n} = |\mathbf{R}_m - \mathbf{R}_n|, \tag{6}$$

$$R_{n\sigma} = \frac{1}{A_n}\sum_{i\in{\rm C}_n}\frac{{\rm Re}Z_{i\sigma}}{\sqrt{\nu_\sigma}}, \tag{7}$$

where A_n is the mass number of cluster ${\rm C}_n$ and the expression $i \in {\rm C}_n$ means that the ith nucleon is contained in cluster ${\rm C}_n$. It should be noted that the $\sigma(=x, y, z)$ component of the spatial center of the single-particle wave function $|\varphi_i\rangle$ is $\frac{{\rm Re}Z_{i\sigma}}{\sqrt{\nu_\sigma}}$. When sufficiently large values are chosen for $v^\beta_{\rm cnst}$ and $v^d_{\rm cnst}$, the resultant values β and $d_{{\rm C}_m\text{-}{\rm C}_n}$ of energy variation become $\tilde{\beta}$ and $\tilde{d}_{{\rm C}_m\text{-}{\rm C}_n}$, respectively. We constrained the $d_{\alpha\text{-}^{36}{\rm Ar}}$ and $d_{^{12}{\rm C}\text{-}^{28}{\rm Si}}$ values for the d constraint. In each calculation of energy variation, we constrained one of β, $d_{\alpha\text{-}^{36}{\rm Ar}}$, and $d_{^{12}{\rm C}\text{-}^{28}{\rm Si}}$. A detailed explanation regarding the d constraint may be found in Ref. [23].

The energy variation with the AMD wave function is carried out using the frictional cooling method [25]. The time evolution equation for the complex parameters $\mathbf{Z}_i$, α_i, and β_i is

$$\frac{dX_i}{dt} = -\mu_X\frac{\partial E^\pi}{\partial X_i^*}, \quad (i = 1, 2, \ldots, A), \tag{8}$$

where X_i is $\mathbf{Z}_i$, α_i, or β_i, and that for the real parameters ν_x, ν_y, and ν_z is

$$\frac{d\nu_\sigma}{dt} = -\mu_\nu \frac{\partial E^\pi}{\partial \nu_\sigma} (\sigma = x, y, z). \tag{9}$$

The quantities μ_X and μ_ν are arbitrary positive real numbers. The energy of the system decreases as time progresses, and after a sufficient number of time steps, we obtain a local minimum energy state.

After the constrained energy variation for $|\Phi^\pi\rangle$, we superposed the optimized wave functions employing the quadrupole deformation parameter β and the distances between the centers of mass among clusters $d_{\mathrm{C}_m\text{-}\mathrm{C}_n}$ for C_m-C_n configurations as the generator coordinate,

$$\left|\Phi^{J^\pi}_M\right\rangle = \sum_K \hat{P}^{J^\pi}_{MK} \left(\sum_i f^\beta_{iK} \left|\Phi^\beta_i\right\rangle + \sum_{i,\mathrm{C}_m\text{-}\mathrm{C}_n} f^{d_{\mathrm{C}_m}\text{-}\mathrm{C}_n}_{iK} \left|\Phi^{d_{\mathrm{C}_m\text{-}\mathrm{C}_n}}_i\right\rangle \right), \tag{10}$$

where $\hat{P}^{J^\pi}_{MK}$ is the parity and total angular momentum projection (AMP) operator, and $|\Phi^\beta_i\rangle$ and $|\Phi^{d_{\mathrm{C}_m\text{-}\mathrm{C}_n}}_i\rangle$ are optimized wave functions with β and $d_{\mathrm{C}_m\text{-}\mathrm{C}_n}$ constraints for the constrained values $\tilde{\beta}^{(i)}$ and $\tilde{d}^{(i)}_{\mathrm{C}_m\text{-}\mathrm{C}_n}$, respectively. The integrals over the three Euler angles in total AMP operator $\hat{P}^J_{MK}$ are evaluated by numerical integration. The mesh widths in numerical integration are $2\pi/17, \pi/65$, and $2\pi/17$ for α, β, and γ, respectively. Here the body-fixed x, y, and z axes are chosen as $\langle x^2\rangle \leqslant \langle y^2\rangle \leqslant \langle z^2\rangle$ for $\gamma < 30^\circ$ wave functions and $\langle x^2\rangle \geqslant \langle y^2\rangle \geqslant \langle z^2\rangle$ for $\gamma > 30^\circ$ ones, respectively. The coefficients f^β_{iK} and $f^{d_{\mathrm{C}_m}\text{-}\mathrm{C}_n}_{iK}$ are determined by the Hill-Wheeler equation,

$$\delta\left(\left\langle\Phi^{J^\pi}_M\middle|\hat{H}\middle|\Phi^{J^\pi}_M\right\rangle - \epsilon\left\langle\Phi^{J^\pi}_M\middle|\Phi^{J^\pi}_M\right\rangle\right) = 0. \tag{11}$$

C. Squared overlap

We defined squared overlap SO to estimate the overlap of a specific model space in the superposed wave function. Suppose the nonorthonormalized wave functions $|\Phi^X_i\rangle$ span the functional space $\{X\}$, for example, $\{X\} = \{|\Phi^\beta_i\rangle\}$, $\{|\Phi^{d_{\alpha\text{-}^{36}\mathrm{Ar}}}_i\rangle\}$, or $\{|\Phi^{d_{^{12}\mathrm{C}\text{-}^{28}\mathrm{Si}}}_i\rangle\}$. Orthonormalized wave functions $|\tilde{\Phi}^X_\alpha\rangle$ are obtained by performing unitary transformations from $|\Phi^X_i\rangle$,

$$\left|\tilde{\Phi}^X_\alpha\right\rangle = u_{\alpha i}\left|\Phi^X_i\right\rangle, \tag{12a}$$

$$\left\langle\tilde{\Phi}^X_\alpha\middle|\tilde{\Phi}^X_\beta\right\rangle = \delta_{\alpha\beta}. \tag{12b}$$

Using the $|\tilde{\Phi}^X_\alpha\rangle$, we define the squared overlap between $|\Phi\rangle$ and the functional space $\{X\}$ as

$$SO = \sum_\alpha \left|\left\langle\tilde{\Phi}^X_\alpha\middle|\Phi\right\rangle\right|^2. \tag{13}$$

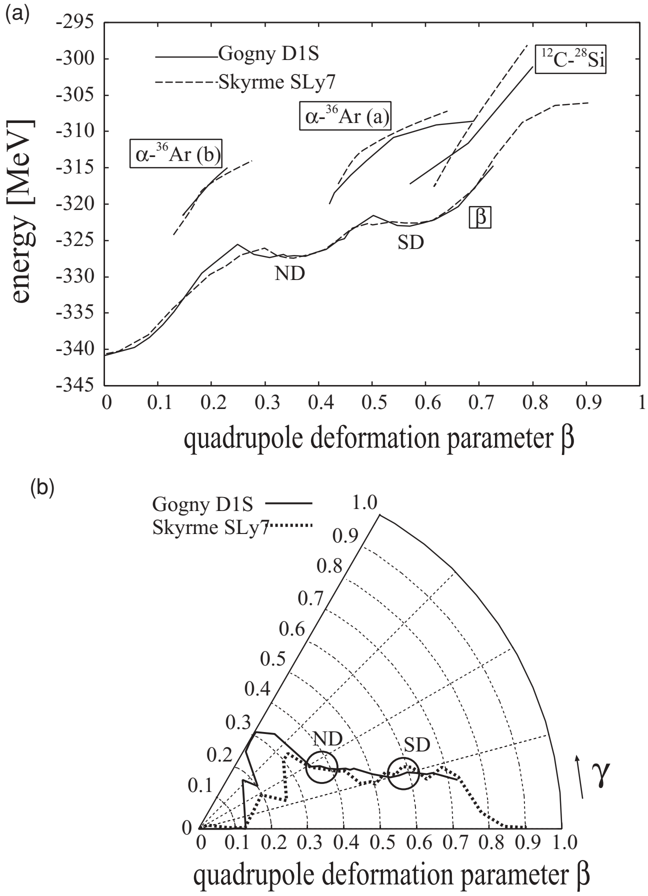

FIG. 1. (a) The energy curves for the positive-parity states obtained using β, $d_{\alpha\text{-}^{36}\mathrm{Ar}}$, and $d_{^{12}\mathrm{C}\text{-}^{28}\mathrm{Si}}$ constraints. The energies are plotted as functions of quadrupole deformation β. The solid (dotted) line shows the results for D1S (SLy7). (b) Projection of the energy curves onto the β-γ plane. The solid (dotted) line shows the results for D1S (SLy7).

III. RESULTS AND DISCUSSIONS

A. Various structures obtained with β and d constraints

We performed the energy variation after the projection to the positive-parity state imposing two different kinds of constraints, β and d constraints.

Figure 1(a) shows the obtained energy curves as a function of matter quadrupole deformation β. By applying the β constraint we obtained energy curves for D1S (solid line) and SLy7 (dotted line). The two forces give quite similar curves that have three local minima or shoulders at $\beta \sim 0$, 0.4, and 0.6. As shown in Table I, they also give approximately the same kinetic and potential energies around each minimum. Therefore, we mainly discuss the D1S result and make some comments on the differences between D1S and SLy7 in the following. The lowest minimum at $\beta = 0$ corresponds to the spherical ground state and the two minima at $\beta \sim 0.4$ and 0.6 correspond to the ND and SD states, respectively. The excitation energies of the ND and SD minima are approximately 14 and 18 MeV, respectively. This result qualitatively agrees with the constrained SHF calculation using SLy4 [19]. However, the energy curve in the constrained SHF-BCS calculation with

TABLE I. Expectation values of kinetic and potential energies around the ground state and ND and SD minima. K, V_{NN}, V_{LS}, and V_C denote kinetic energy, central, spin-orbit, and Coulomb potentials, respectively.

Interaction	β	Total	K	V_{NN}	V_{LS}	V_C
D1S	0.00	−340.9	634.2	−1046.2	−0.1	71.2
SLy7	0.00	−340.7	637.9	−1050.0	0.0	71.5
D1S	0.39	−326.7	654.6	−1033.7	−18.4	70.9
SLy7	0.39	−326.8	653.7	−1031.9	−19.4	70.8
D1S	0.62	−322.2	670.9	−1029.9	−33.6	70.4
SLy7	0.61	−322.3	676.2	−1035.9	−33.3	70.7

SLy6 [20] reveals different behavior. It has neither a ND minimum nor a shoulder, but it does have a SD minimum. The excitation energy of the SD minimum is much smaller than ours and that of Ref. [19]. This difference may be due to the strong pairing correlation reported in Ref. [20].

In the present calculation, we do not make any assumptions regarding the spatial symmetry of the wave function nor put any constraints on the quadrupole deformation γ. Therefore γ has the optimal value for each given value of β.

Figure 1(b) shows the projection of the energy curve onto the β-γ plane. It shows that in most regions the system is triaxially deformed and the degree of the triaxial deformation greatly changes as a function of β. Starting from the spherical ground state, the system rapidly changes to oblate deformation around $\beta = 0.15$–0.25 via a small prolate deformation. Then, it changes to triaxial deformation around $\beta = 0.35$ where the ND minimum appears and the system has the largest triaxiality. With a further increase of β, γ decreases gradually from $\gamma = 30^\circ$ at $\beta = 0.35$ to $\gamma = 15^\circ$ at $\beta = 0.70$. The SD minimum that appears at $\beta = 0.60$ also has a large triaxial deformation $\gamma = 15^\circ$. The deformation of the $\beta - \gamma$ curve for SLy7 shows similar behavior except in the region of $\beta = 0.15$–0.30. In the $\beta \sim 0.30$ region, the deformation obtained for SLy7 is triaxial, which is different from the oblate deformation with D1S. The wave functions in this region did not affect the ND and SD bands, nor their side bands as shown later.

Figure 2 shows the density distribution of the ND and SD minima and confirms their large triaxial deformation. It also reveals the deformed mean-field nature of the ND minimum and implies the existence of a relationship between the SD minimum and the cluster structure. At the limit when all $\mathbf{Z_i} \to \mathbf{0}$ (all centroids of single-particle wave packets go to the origin of the coordinate frame), the AMD wave function is identical to an eigenstate of the deformed harmonic oscillator whose oscillation number is given by the relation $\omega_\sigma = 2\hbar\nu_\sigma/M$. In contrast, when the system has a cluster-like structure, the $\mathbf{Z_i}$ are separated into several groups to describe cluster subunits. In the case of the ND minimum, the centroids of the single-particle wave packets are located around the origin and the wave packets are strongly deformed, $(\nu_x, \nu_y, \nu_z) = (0.16, 0.14, 0.11)$, suggesting that the nature of the mean field is deformed. In the case of the SD minimum, the wave packets are further deformed, $(\nu_x, \nu_y, \nu_z) = (0.17, 0.15, 0.10)$, and reveal the aspect of a triaxially deformed mean field. In the case of the SD minimum, the centroids of the single-particle wave packets appear separated into two $(28 + 12)$ or three $[(12 + 16) + 12]$ groups and the density distribution reveals an octupole deformation, implying that the SD minimum also has an asymmetric cluster-like nature. It will be shown using the d constraint that this has a significant overlap with the ^{12}C-^{28}Si cluster structure.

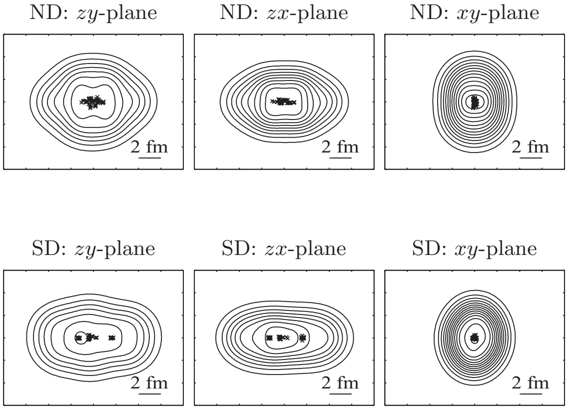

FIG. 2. Density distributions of the ND and SD minima obtained using the β constraint. The crosses in the figure show the centroids of the wave packets. The deformation parameters are $(\beta, \gamma) = (0.39, 25.2^\circ)$ and $(0.62, 14.5^\circ)$ for the ND and SD minima, respectively.

There are few studies on the triaxial deformation of ^{40}Ca, but some theoretical work has suggested the triaxiality of the ND [7,8] and SD [19] states. The present calculation with the β constraint has shown that most of the states on the energy curve have a triaxial deformation. We therefore consider it indispensable to study the issue without the assumption of spatial symmetry to understand the excited states of ^{40}Ca.

With the β constraint, we do not find spatially developed clustering at the ND and SD minima, although the density distribution of the SD state implies its relationship to clustering. We have therefore applied the d constraint. We discuss the results obtained with $d_{\alpha\text{-}^{36}\mathrm{Ar}}$ and $d_{^{12}\mathrm{C}\text{-}^{28}\mathrm{Si}}$ constraints. Other combinations of clusters such as 2α-^{32}Si have also been applied, but they have appeared at comparatively high excitation energy levels and were not involved with the ND and SD states even after the GCM calculation.

By applying the $d_{\alpha\text{-}^{36}\mathrm{Ar}}$ constraint, we have obtained an excited energy curve above the energy curve obtained with the β constraint (Fig. 1). Two different kinds of structure appeared on the energy curve. In both cases, the system has well-developed α-^{36}Ar cluster structures, as may be clearly seen in their density distributions [Figs. 3(a) and 3(b)]. The difference between them is the orientation of the axis of symmetry in the oblately deformed ^{36}Ar cluster. The first is denoted as type (a). In this type, the axis of symmetry for ^{36}Ar is perpendicular to the vector that connects the α and ^{36}Ar clusters. Therefore the whole system has a triaxial deformation. This type of structure is favored under $d_{\alpha\text{-}^{36}\mathrm{Ar}}$ constraints with large $d_{\alpha\text{-}^{36}\mathrm{Ar}}$ values and appears in the region of $\beta = 0.45$–0.7. The second kind of structure is denoted type (b). In this type, the axis of symmetry in the ^{36}Ar cluster is parallel to the vector that connects the α and ^{36}Ar clusters, resulting in an axial deformation of the system. This type is

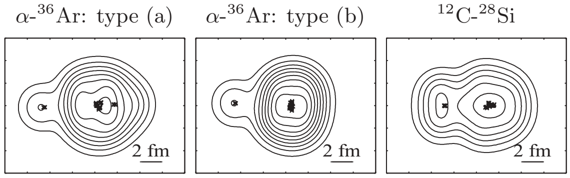

FIG. 3. Density distributions of intrinsic states obtained with the d constraint. $d_{\alpha\text{-}^{36}\mathrm{Ar}}$ is fixed to 5.0 fm for α-^{36}Ar (a) and (b). $d_{^{12}\mathrm{C}\text{-}^{28}\mathrm{Si}}$ is fixed to 4.0 fm for ^{12}C-^{2}Si. The crosses in the figure show the centroids of the wave packets.

obtained when the intercluster distance is restricted to a shorter distance ($d_{\alpha\text{-}^{36}\mathrm{Ar}} = 4.5$–$5.5$ fm) and appears in the region of $\beta = 0.15$–0.3. It is interesting that type (b) is bound deeper than type (a) for shorter intercluster distances and ^{36}Ar changes its orientation as the intercluster distance becomes larger. We assume that ^{36}Ar changes its orientation to make the overlap and potential energy between the α and ^{36}Ar clusters larger.

By applying a $d_{^{12}\mathrm{C}\text{-}^{28}\mathrm{Si}}$ constraint ($d_{^{12}\mathrm{C}\text{-}^{28}\mathrm{Si}} = 4.0$–$6.0$ fm), we obtained a strongly deformed and excited energy curve that appears in the region of $\beta = 0.55$–0.8. The system has a prominent ^{12}C-^{28}Si cluster structure and is triaxially deformed, as shown in Fig. 3. In this case, we did not find a change in the orientation of the clusters.

The d constraints have generated excited energy curves in which the system has prominent cluster structures. The fact that these wave functions are mixed with the wave functions obtained with the β constraint and play an important role in describing highly excited bands is discussed in the following.

B. Angular momentum projection

The wave functions just obtained are projected onto the eigenstate of the total angular momentum. The $J^\pi = 0^+$ and 2^+ states obtained with the β constraint are shown in Fig. 4. For $J^\pi = 2^+$ states, different K states are superposed by diagonalizing Hamiltonian and norm matrices as

$$\left|\Phi^{J+M}_{\mathrm{AMP}}(\beta)\right\rangle = \sum_K f_K^{\mathrm{AMP}} \hat{P}^J_{MK} |\Phi^+(\beta)\rangle. \tag{14}$$

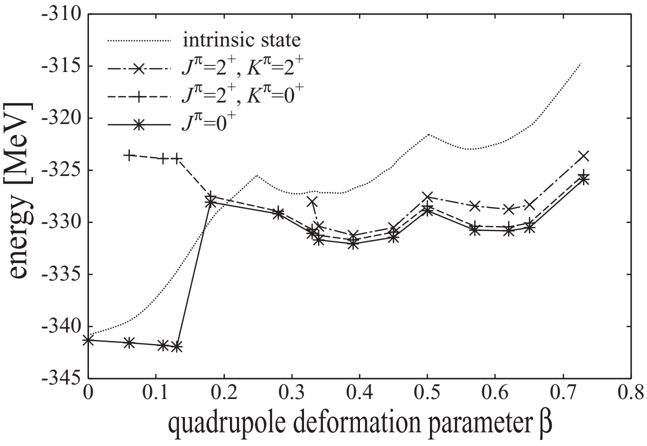

FIG. 4. The energy curves of the $J^\pi = 0^+$ and 2^+ states projected from wave functions obtained with the β constraint with D1S.

TABLE II. Squared overlaps of the K component, $SO(K)$, in the $J^\pi = 2^+$ states $|\Phi_{\mathrm{AMP}^{J+\mathrm{M}}(\beta)}\rangle$ projected from $\beta = 0.39$ and 0.62 wave functions. The labels "$K^\pi = 0^+$" and "$K^\pi = 2^+$" indicate the dominant K component.

β	K^π	$SO(K=0)$	$SO(K=-2)$	$SO(K=2)$
0.39	"$K^\pi = 0^+$"	0.999	0.002	0.003
	"$K^\pi = 2^+$"	0.001	0.989	0.990
0.62	"$K^\pi = 0^+$"	1.00	0.000	0.000
	"$K^\pi = 2^+$"	0.001	0.982	0.985

AMP reduces the excitation energies of the deformed states. For example, the $J^\pi = 0^+$ states of ND and SD are lowered by approximately 6 and 9 MeV, respectively. As a result, they almost degenerate in terms of energy. In the deformed region, we have obtained two low-lying 2^+ states for each given value of β by the diagonalization with K. These states are denoted as $K^\pi = 0^+$ and 2^+ according to the K-dominant component of their wave function.

In Table II, squared overlaps of the K component,

$$SO(K,\beta) \equiv \frac{\left|\langle\Phi^+(\beta)|\left(\hat{P}^J_{MK}\right)^\dagger\left|\Phi^{J+M}_{\mathrm{AMP}}(\beta)\right\rangle\right|^2}{\langle\Phi^+(\beta)|\hat{P}^J_{KK}|\Phi^+(\beta)\rangle\left\langle\Phi^{J+M}_{\mathrm{AMP}}(\beta)\middle|\Phi^{J+M}_{\mathrm{AMP}}(\beta)\right\rangle}, \tag{15}$$

are shown. It is found that different $|K|$ states hardly mix with each other, and almost pure $|K|$ states are found after the diagonalization. Therefore, K can be regarded as a good quantum number. Although K distributions are slightly distorted after GCM calculation, K mixing is small and K is an appropriately good quantum number.

The presence of the $K^\pi = 2^+$ state is due to the triaxial deformation in the $\beta \gtrsim 0.3$ region. As will be discussed in the following, the triaxial deformations of the ND and SD states leads to the presence of their side bands, $K^\pi = 2^+$.

The energy of the wave functions obtained with the d constraint are also lowered by AMP. The α-^{36}Ar type (a) and (b) and ^{12}C-^{28}Si states are lowered by approximately 5–10, 10–15, and 10 MeV, respectively. α-^{36}Ar type (a) and ^{12}C-^{28}Si wave functions have the $K^\pi = 2^+$ components because of the triaxial deformation.

C. GCM calculation

1. *Energy levels and deformations*

After applying the AMP, we carried out GCM calculations. For the GCM basis, we adopted 15 β-constrained wave functions $\beta = 0.00$–0.73 and $7 d_{\alpha\text{-}^{36}\mathrm{Ar}}$-constrained wave functions of type (a) with $d_{\alpha\text{-}^{36}\mathrm{Ar}} = 4.5$–$9.0$ fm. In the superpositions, we adopted projected states with $|K| \leqslant 4$ and $\langle\Phi^+|\hat{P}^J_{KK}|\Phi^+\rangle/\langle\Phi^+|\Phi^+\rangle > 0.005$ states. We omitted other states with $|K| > 4$ or small norm because they may contain numerical errors in the numerical integration of AMP. We checked convergence of the energy levels with respect to the number of basis wave functions along β and the α-^{36}Ar surface by comparing the energies calculated by the full set of basis wave functions and a reduced set. For example, we

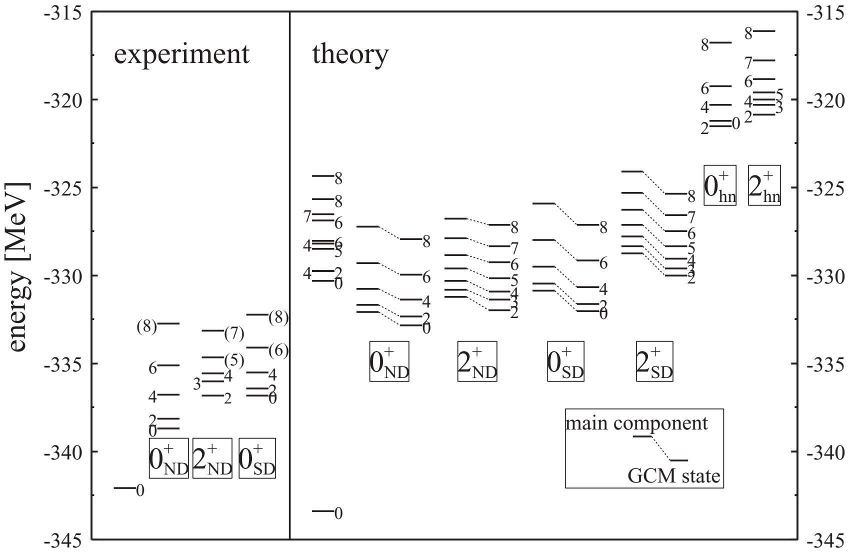

FIG. 5. Energy levels in ^{40}Ca. The left-hand side represents experimental values, and the right-hand side theoretical values. The energies of superposed wave functions and that of the main component are represented.

calculated the energies with a reduced set of basis by adopting 7 β-constrained wave functions and 7$d_{\alpha\text{-}^{36}\mathrm{Ar}}$-constrained type (a) wave functions, and we found that the difference from energies for the full set is less than 1 MeV. In addition to the β- and $d_{\alpha\text{-}^{36}\mathrm{Ar}}$-constrained type (a) wave functions, we also adopted 3 $d_{\alpha\text{-}^{36}\mathrm{Ar}}$-constrained wave functions of type (b) with $d_{\alpha\text{-}^{36}\mathrm{Ar}} = 4.5$–$5.5$ fm and 3$d_{^{12}\mathrm{C}\text{-}^{28}\mathrm{Si}}$-constrained wave functions with $d_{^{12}\mathrm{C}\text{-}^{28}\mathrm{Si}} = 4.0$–$6.0$ fm in the superposition. Then we obtained the final GCM wave functions by diagonalizing Hamiltonian and norm matrices for the parity and angular momentum projected states with the 28 independent wave functions.

The theoretical energy levels of the GCM states and the experimental levels are shown in Fig. 5. The energies of the simple AMP for the main components for low-lying bands are also given. In most levels, the GCM states gain approximately 1 MeV from the simple AMP. Experimentally, the $K^\pi = 0^+, 2^+$, and 0^+ bands built on $J^\pi = 0^+_2, 2^+_1$, and 0^+_3 states are known to be the ND band ($K^\pi = 0^+_{\mathrm{ND}}$)m the side band of the ND band ($K^\pi = 2^+_{\mathrm{ND}}$), and the SD band ($K^\pi = 0^+_{\mathrm{SD}}$). In the GCM calculation, we obtained two $K^\pi = 0^+$ and two $K^\pi = 2^+$ bands and some states in low-lying states above the ground state. We assigned the first and second $K^\pi = 0^+$ bands to the observed $K^\pi = 0^+_{\mathrm{ND}}$ and 0^+_{SD} bands, respectively, and the first $K^\pi = 2^+$ band to the observed $K^\pi = 2^+_{\mathrm{ND}}$ band, because the theoretical moments of inertia and electric transition strength $B(E2)$ of these bands correlate well with the experimental data for the corresponding bands, as discussed in the following. The second $K^\pi = 2^+$ band in the results is regarded as the side band $K^\pi = 2^+_{\mathrm{SD}}$ of the SD band. We also obtained the $K^\pi = 0^+$ and 2^+ bands in highly excited states with large α-^{36}Ar cluster structure components, which are the candidates for α-^{36}Ar higher nodal bands, $K^\pi = 0^+_{\mathrm{hn}}$ and 2^+_{hn}, observed experimentally [15].

Let us consider the GCM results of the low-lying states (ground, ND, and SD states) in more detail by analyzing the squared overlap between $J^\pi = 0^+$ states and the AMP states from the β-constrained wave functions. The ND state's $K^\pi = 0^+_{\mathrm{ND}}$ and 2^+_{ND} bands are mainly constructed from the β-constrained wave functions around the ND minimum occurring in the $\beta \sim 0.4$ region. The members of ND bands have a maximum overlap of approximately 85% for the triaxially deformed state with $(\beta, \gamma) = (0.39, 25.2^\circ)$. There is no mixing between the ND state and the ground state. The squared overlap with the β-constrained wave functions is almost unchanged up to high spin states along the $K^\pi = 0^+_{\mathrm{ND}}$ band. However, in the $K^\pi = 2^+_{\mathrm{ND}}$ band, the squared overlap of each component changes with the increase in spin, which implies the change of structure in this band. In the GCM calculation, the theoretical excitation energies of the members of SD bands in the $K^\pi = 0^+_{\mathrm{ND}}$ and 2^+_{ND} bands are 10.5 and 11.4 MeV, respectively. These are much higher than the experimental excitation energies.

However, kinematic moments of inertia $\mathcal{J}^{(1)}$ in $K^\pi = 0^+_{\mathrm{ND}}$ and 2^+_{ND} bands reasonably agree with those of experimental data, as shown in Fig. 6. Namely, the averaged theoretical $\mathcal{J}^{(1)}$ value for ND states is approximately $7\hbar^2$/MeV, and the value is consistent with the experimental values.

The SD states, $K^\pi = 0^+_{\mathrm{SD}}$ and 2^+_{SD}, are constructed mainly by β-constrained wave functions around the SD local minimum. The main component is the β-constrained wave function with triaxial shape, $(\beta, \gamma) = (0.62, 14.5^\circ)$. The squared overlap is more than 90% in the bandhead states and remains almost unchanged up to high spin states along the $K^\pi = 0^+_{\mathrm{SD}}$ and 2^+_{SD} bands. A small degree of mixing between the ND and SD bands is seen in the $\beta \sim 0.5$ region. The GCM calculation reveals the bandhead energies of the $K^\pi = 0^+_{\mathrm{SD}}$ and 2^+_{SD} bands as 11.4 and 13.4 MeV, respectively. Although the present calculations overestimate experimental excitation energies of the $K^\pi = 0^+_{\mathrm{SD}}$ band as well as the ND bands, the theoretical $\mathcal{J}^{(1)}$ values for SD states are in good agreement with the experimental data, as shown in Fig. 6.

We comment on comparison of our results with those of other theoretical studies. In spherical-basis AMD [21], $K^\pi = 2^+_{\mathrm{ND}}$ and 2^+_{SD} bands were not obtained, suggesting that deformation of wave packets adopted in the present work is important for describing triaxial deformation. In SHF-BCS + GCM [20], although the excitation energies of the $J^\pi = 0^+_2$

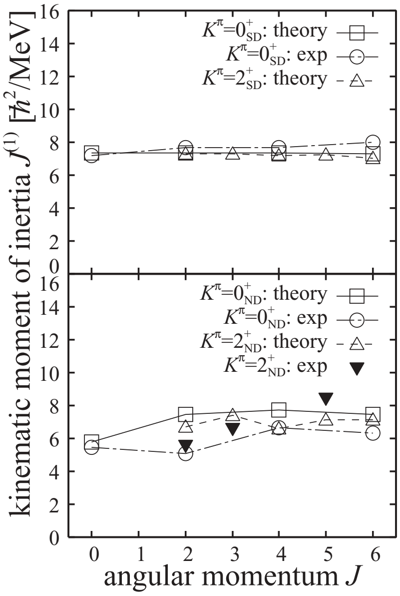

FIG. 6. The kinematic moments of inertia $\mathcal{J}^{(1)}$ in ND and SD states as functions of the angular momentum J. Upper and lower panels are for ND and SD states, respectively.

state and the members of $K^\pi = 0^+_{\mathrm{SD}}$ band were produced, $K^\pi = 2^+$ bands were not obtained because axial symmetry was *a priori* assumed. Moreover, the moment of inertia of the $K^\pi = 0^+_{\mathrm{ND}}$ band could not be reproduced. In α-^{36}Ar OCM [13], the $K^\pi = 0^+_{\mathrm{ND}}$ and 2^+_{ND} bands were reproduced, but the SD band was not described.

2. *Cluster components*

In this section we discuss the contribution of the cluster wave functions in the ND and SD states. In Table III, we list the squared overlap values of the GCM states with the α-^{36}Ar configuration space given by the set of $d_{\alpha\text{-}^{36}\mathrm{Ar}}$-constrained wave functions, and those with the ^{12}C-^{28}Si configuration space, as well as the SO values for the model space of the β-constrained wave functions. The definition of the specific functional space is explained in Sec. II C. The squared overlap between the ND state and β-constrained wave functions is 99%. This means that the ND state is practically represented by the β-constrained wave functions alone. Nonetheless, it is surprising that the ND states have a significant overlap of approximately 40% with the $d_{\alpha\text{-}^{36}\mathrm{Ar}}$-constrained wave functions as well. This indicates that the β-constrained wave functions for the ND states include the α-^{36}Ar component, though the spatially developed cluster structure is not seen in the density distributions. The α-^{36}Ar cluster component in the ND band is mainly consistent with type (a) wave functions, whereas the squared overlap of type (b) wave functions in ND states is almost negligible. The result—that the ND state contains an α-^{36}Ar cluster structure component—is associated with the results of the α-^{36}Ar potential model calculation [10,11], ^{36}Ar(^{6}Li,d)^{40}Ca reaction [14,15], and α-^{36}Ar OCM calculation [13].

TABLE III. The squared overlap (SO) of β-constrained wave functions and d-constrained wave functions.

	K^π	J^π	β constraint SO	d constraint	
				SO	configuration
ND	0^+_{ND}	0^+	0.99	0.37	α-^{36}Ar
		2^+	0.99	0.40	
		4^+	0.99	0.41	
	2^+_{ND}	2^+	0.99	0.41	
		3^+	0.99	0.45	
		4^+	0.99	0.42	
SD	0^+_{SD}	0^+	0.95	0.59	^{12}C-^{28}Si
		2^+	0.95	0.59	
		4^+	0.95	0.58	
	2^+_{SD}	2^+	0.95	0.61	
		3^+	0.95	0.61	
		4^+	0.95	0.60	
α-^{36}Ar higher nodal	0^+_{hn}	0^+	0.50	0.40	α-^{36}Ar
		2^+	0.49	0.47	
		4^+	0.63	0.33	
	2^+_{hn}	2^+	0.54	0.39	
		3^+	0.50	0.47	
		4^+	0.55	0.41	

The SD states are dominated by the β-constrained wave function as well as the ND states. However, the SD states also have a large overlap with the $d_{^{12}\mathrm{C}\text{-}^{28}\mathrm{Si}}$-constrained wave functions, as reflected by the SO of approximately 60%. We found that the β-constrained AMD wave functions for the SD states also include the cluster components, even though the cluster structure is not visible in the density distributions. The ^{12}C-^{28}Si cluster configurations also make a significant contribution to the energy of the SD states. In particular, the energies of the SD states gain approximately 1 MeV owing to the mixing of ^{12}C-^{28}Si cluster structure wave functions. This is associated with the results of spherical-basis AMD [21] according to which the SD states have a ^{12}C-^{28}Si cluster structure configuration.

3. *α-^{36}Ar higher nodal states, $K^\pi = 0^+_{\mathrm{hn}}$ and 2^+_{hn} bands*

As shown in Fig. 5, we obtained $K^\pi = 0^+$ and 2^+ bands with large α-^{36}Ar cluster components in the excitation energy region approximately 10 MeV higher than the ND band. The main component of the higher α-^{36}Ar bands, $K^\pi = 0^+_{\mathrm{hn}}$ and 2^+_{hn}, are $d_{\alpha\text{-}^{36}\mathrm{Ar}}$-constrained wave functions obtained with a large distance, $d_{\alpha\text{-}^{36}\mathrm{Ar}} = 6.0$ fm. We assume that this corresponds to the α-^{36}Ar higher nodal band observed with the ^{36}Ar(^{6}Li,d)^{40}Ca reaction [15], where the fragments of the $J^\pi = 0^+$ state for this band were reported around 8 MeV above the bandhead of the ND band.

The squared overlap between $d_{\alpha\text{-}^{36}\mathrm{Ar}}$-constrained wave functions and the $J^\pi = 0^+$ states in $K^\pi = 0^+_{\mathrm{ND}}$ and 0^+_{hn} bands are shown in Fig. 7. The squared overlap for 0^+_{hn} is suppressed in the small $d_{\alpha\text{-}^{36}\mathrm{Ar}}$ region and has a peak at $d_{\alpha\text{-}^{36}\mathrm{Ar}} = 6$ fm, which demonstrates the nodal property of the intercluster motion in this band. It can be assumed that the α-^{36}Ar higher nodal states arise from the intercluster excitation built on the ND states. In other words, the significant component of the α-^{36}Ar cluster structure in the ND states must be essential for

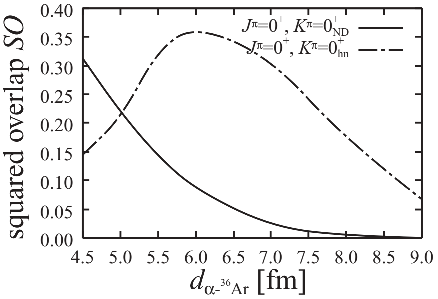

FIG. 7. The squared overlap of the $J^\pi = 0^+$ states in the ND band ($K^\pi = 0^+_{\mathrm{ND}}$) and the α-^{36}Ar higher nodal band ($K^\pi = 0^+_{\mathrm{hn}}$) with $d_{\alpha\text{-}^{36}\mathrm{Ar}}$-constrained wave functions.

the formation of the higher nodal states, because the cluster component in the small-distance region is possible if the ND states contain no cluster component. This means that the higher nodal states appear as a consequence of the orthogonality to the cluster components with a small distance d, which are already contained in the ND states. This situation is similar to the relationship between the ground band and α-^{40}Ca higher nodal band in ^{44}Ti suggested by Kimura and Horiuchi with deformed-basis AMD [27].

4. *Electric transitions*

Here, we investigate the electric quadrupole strengths and discuss the band structure.

The theoretical and experimental values of $E2$ transition strengths $B(E2)$ are shown in Fig. 8. The $B(E2)$ values for intraband transitions are remarkably strong, and the transitions between the $K^\pi = 0^+_{\mathrm{ND}}$ and $K^\pi = 2^+_{\mathrm{ND}}$ bands and those between the $K^\pi = 0^+_{\mathrm{SD}}$ and 2^+_{SD} bands are also strong. This reflects the side-band features of the $K^\pi = 2^+_{\mathrm{ND}}$ and $K^\pi = 2^+_{\mathrm{SD}}$ bands, corresponding to $K^\pi = 0^+_{\mathrm{ND}}$ and $K^\pi = 0^+_{\mathrm{SD}}$, respectively. The interband transitions between ND and SD states and those from ND or SD states to the ground state are underestimated. This is because mixing of wave functions among these bands is small in our calculation.

Detailed comparisons between the theoretical values and experimental data of the $B(E2)$ values are shown in Table IV. The $B(E2)$ values for the intraband transitions in the ND and SD states are reproduced well, except for the $6^+ \to 4^+$ transition when $K^\pi = 0^+_{\mathrm{ND}}$. The small value of the experimental $B(E2; 6^+ \to 4^+)$ is overestimated by the calculation, although the error in the experimental value is rather large.

We also compared our results with those of other theoretical studies in Table IV. The $B(E2)$ values in (4) α-^{36}Ar OCM are consistent with the present values for the ND states. This may indicate that the deformation of the ND states in our calculations is similar to that calculated with the α-^{36}Ar cluster model. In (1) the spherical-basis AMD, $B(E2)$ values in $K^\pi = 0^+_{\mathrm{ND}}$ and 0^+_{SD} bands are underestimated, whereas our results are consistent with experimental values. This means that deformation of wave packets works well for quantitatively describing the deformed states of ^{40}Ca. In (3) the shell model, smaller $B(E2)$ values for the $K^\pi = 0^+_{\mathrm{ND}}$ and 0^+_{SD} bands were obtained by comparison to our model. In (2) SHF-BCS + GCM, the $B(E2)$ values are also smaller than our results for $K^\pi = 0^+_{\mathrm{ND}}$ and 0^+_{SD} bands. In particular, the $B(E2)$ value for the $4^+ \to 2^+$ transition in both the ND and SD states is remarkably small. This shows that the ND and SD bands obtained in the SHF-BCS + GCM calculation are not rigid-rotor-like. This seems to be inconsistent with experimental results regarding the rigid-rotor-like property, which has been found in rotational energies and $E2$ transitions. Further analysis requires more detailed measurements of the $E2$ transition strengths.

IV. SUMMARY

We investigated the ground state and excited states of ^{40}Ca in the framework of deformed-basis AMD, focusing on the aspects of triaxiality and clustering in the deformed states. Superposing mean-field-type and cluster-structure-type wave functions obtained with β and d constraints, respectively, we obtained the ground states and ND, SD, and α-^{36}Ar higher-nodal states. We found that both the ND and SD bands are constructed from triaxially deformed shapes, and

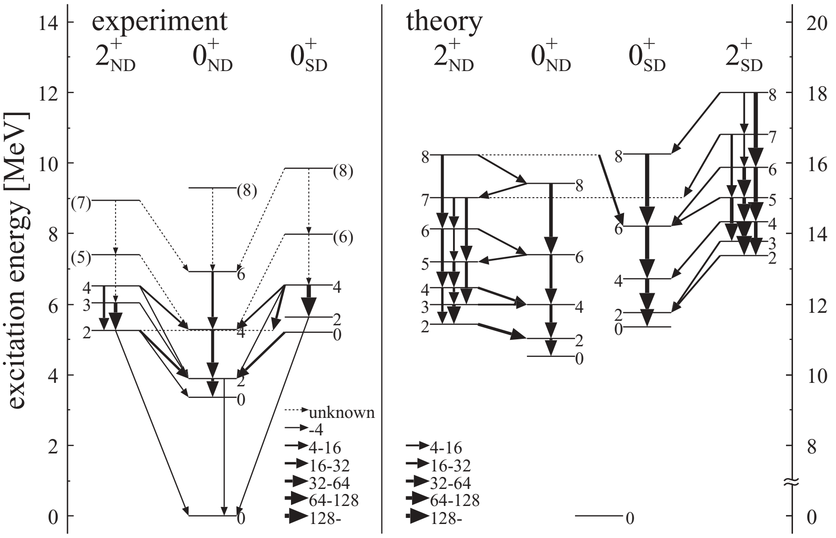

FIG. 8. Experimental and theoretical $B(E2)$ values in Weisskopf units: $B(E2)_{\mathrm{W.u.}} = 8.12e^2\ \mathrm{fm}^4$ for ^{40}Ca. In theoretical values, transitions stronger than $4B(E2)_{\mathrm{W.u.}}$ are presented. The experimental data are taken from Refs. [13] and [26]. A transition marked "unknown" indicates that the transition has been observed but $B(E2)$ has not been measured.

TABLE IV. Theoretical and experimental $B(E2)$ of ^{40}Ca. The units of transitions are Weisskopf units: $B(E2)_{\mathrm{W.u.}} = 8.12e^2$ fm^4. Experimental $B(E2)$ values taken from Refs. [13] and [22] are marked by single and double asterisks, respectively; all other values are taken from Ref. [26]. (1), (2), (3), and (4) are result of spherical-basis AMD [21], HF-BCS + GCM [20], shell model [22], and α-^{36}Ar OCM [13], respectively.

$K_i^\pi \rightarrow K_f^\pi$	I_i	I_f	Experimental	Present work	(1)	(2)	(3)	(4)
$0^+_{\mathrm{ND}} \rightarrow$ g.s.	2^+	0^+	2.26 ± 0.14	<0.01			0.22	0.025
$2^+_{\mathrm{ND}} \rightarrow$ g.s.	2^+	0^+	0.13 ± 0.04	<0.01			0.025	0.001
$0^+_{\mathrm{SD}} \rightarrow$ g.s.	2^+	0^+	0.20 ± 0.05	<0.01			0.01	
$0^+_{\mathrm{ND}} \rightarrow 0^+_{\mathrm{ND}}$	2^+	0^+	32 ± 4	39.13	7.9	13.8	36.0	33.4
	4^+	2^+	61 ± 10	55.03	14.3	2.0	48.9	48.1
	6^+	4^+	17^{+9}_{-17}	61.24	15.8	23.0	42.6	52.9
	8^+	6^+	—	64.36	24.6		28.0	53.8
$0^+_{\mathrm{SD}} \rightarrow 0^+_{\mathrm{SD}}$	2^+	0^+	—	118.47	40.6	55.0	71.3	
	4^+	2^+	170 ± 40	169.54	58.9	45.9	100	
	6^+	4^+	—	186.53	56.0	68.6	108	
	8^+	6^+	—	178.82	38.1	109	112	
$2^+_{\mathrm{ND}} \rightarrow 2^+_{\mathrm{ND}}$	3^+	2^+	$>71, 82 \pm 26^*$	66.66			52.6	61.6
	4^+	2^+	$23 \pm 5^*$	20.76			16.4	19.3
	4^+	3^+	$<1300^*$	29.24			35.0	43.3
$2^+_{\mathrm{ND}} \rightarrow 0^+_{\mathrm{ND}}$	2^+	0^+	$1.3 \pm 0.4, 0.54 \pm 0.14^*$	0.015			2.0	7.0
	2^+	2^+	$22 \pm 6, 25 \pm 6^*$	44.30			11	11.3
	3^+	2^+	$3.7 \pm 0.7^*$	0.064			3.4	12.4
	3^+	4^+	$<22^*$	15.49				7.3
	4^+	2^+	3.8 ± 0.8	0.28			2.5	3.5
	4^+	4^+	$6.8 \pm 5.2^*$	16.65			6.0	13.6
$0^+_{\mathrm{SD}} \rightarrow 0^+_{\mathrm{ND}}$	0^+	2^+	17 ± 3	0.080			7.1	
	2^+	0^+	2.6 ± 0.7	<0.01			0.4	
	4^+	2^+	2.6 ± 0.6	0.017			2.4	
	4^+	4^+	$14.3 \pm 4.2^{**}$	<0.01			0.83	
$0^+_{\mathrm{SD}} \rightarrow 2^+_{\mathrm{ND}}$	4^+	2^+	22 ± 6	0.018				

we obtained the $K^\pi = 2^+$ side bands of these bands. The theoretical $B(E2)$ and moments of inertia are consistent with experimental data, although the excitation energies are higher than empirical values. In the spherical-basis AMD calculation [21], the $K^\pi = 2^+_{\mathrm{ND}}$ band has not been obtained, and $B(E2)$ intraband values in $K^\pi = 0^+_{\mathrm{ND}}$ and 0^+_{SD} bands are underestimated. This shows that the deformed-basis AMD is essential for describing triaxial deformation and useful for the quantitative description of $B(E2)$.

The ND band and its side band contain approximately 40% of the α-^{36}Ar cluster structure component, and the SD band and its side band contain approximately 60% of the ^{12}C-^{28}Si cluster structure component. The α-^{36}Ar higher nodal band was obtained from the excitation of intercluster motion between the α and ^{36}Ar clusters. The present results suggest that cluster correlation will be important for deformation and excitation even in medium- and heavy-weight nuclei.

ACKNOWLEDGMENTS

The authors would like to thank Dr. Inakura and Dr. Fujiwara for fruitful discussions. The numerical calculations were carried out on SX8 at YITP, Kyoto University, and on SX5 and SX8 at RCNP, Osaka University. This work has been supported by a JSPS research grant for young scientists and by a Grant-in-Aid for the 21st Century COE "Center for Diversity and Universality in Physics" from the Ministry of Education, Culture, Sports, Science and Technology of Japan (MEXT).

---

[1] H. Horiuchi, K. Ikeda, and Y. Suzuki, Prog. Theor. Phys. Suppl. **52**, 89 (1972), and references therein.

[2] Y. Fujiwara, H. Horiuchi, K. Ikeda, M. Kamimura, K. Katō, Y. Suzuki, and E. Uegaki, Prog. Theor. Phys. Suppl. **68**, 29 (1980), and references therein.

[3] F. Michel, S. Ohkubo, and G. Reidemeister, Prog. Theor. Phys. Suppl. **132**, 7 (1998), and references therein.

[4] T. Sakuda and S. Ohkubo, Prog. Theor. Phys. Suppl. **132**, 103 (1998), and references therein.

[5] T. Yamaya, K. Katori, M. Fujiwara, S. Kato, and S. Ohkubo, Prog. Theor. Phys. Suppl. **132**, 73 (1998), and references therein.

[6] W. J. Gerace and A. M. Green, Nucl. Phys. **93**, 110 (1967).

[7] W. J. Gerace and A. M. Green, Nucl. Phys. **A123**, 241 (1969).

[8] W. J. Gerace and J. P. Mestre, Nucl. Phys. **A285**, 253 (1977).

[9] K. F. Pal and R. G. Lovas, Phys. Lett. **B96**, 19 (1980).

[10] S. Ohkubo and K. Umehara, Prog. Theor. Phys. **80**, 598 (1988).

[11] G. Reidemeister, S. Ohkubo, and F. Michel, Phys. Rev. C **41**, 63 (1990).

[12] T. Ogawa, Y. Suzuki, and K. Ikeda, Prog. Theor. Phys. **57**, 1072 (1977).

[13] T. Sakuda and S. Ohkubo, Phys. Rev. C **49**, 149 (1994).

[14] T. Yamaya, M. Saito, M. Fujiwara, T. Itahashi, K. Katori, T. Suehiro, S. Kato, S. Hatori, and S. Ohkubo, Phys. Lett. **B306**, 1 (1993).

[15] T. Yamaya, M. Saitoh, M. Fujiwara, T. Itahashi, K. Katori, T. Suehiro, S. Kato, S. Hatori, and S. Ohkubo, Nucl. Phys. **A573**, 154 (1994).

[16] R. Middleton, J. D. Garrett, and H. T. Fortune, Phys. Lett. **B39**, 339 (1972).

[17] J. R. MacDonald, D. H. Wilkinson, and D. E. Alburger, Phys. Rev. C **3**, 219 (1971), and references therein.

[18] E. Ideguchi *et al.*, Phys. Rev. Lett. **87**, 222501 (2001).

[19] T. Inakura, S. Mizutori, M. Yamagami, and K. Matsuyanagi, Nucl. Phys. **A710**, 261 (2002).

[20] M. Bender, H. Flocard, and P.-H. Heenen, Phys. Rev. C **68**, 044321 (2003).

[21] Y. Kanada-En'yo and M. Kimura, Phys. Rev. C **72**, 064322 (2005).

[22] E. Caurier, J. Menendez, F. Nowacki, and A. Poves, Phys. Rev. C **75**, 054317 (2007).

[23] Y. Taniguchi, M. Kimura, and H. Horiuchi, Prog. Theor. Phys. **112**, 475 (2004).

[24] A. Dote, H. Horiuchi, and Y. Kanada-En'yo, Phys. Rev. C **56**, 1844 (1997).

[25] Y. Kanada-Enyo and H. Horiuchi, Prog. Theor. Phys. **93**, 115 (1995).

[26] J. A. Cameron and B. Singh, Nucl. Data Sheets **102**, 293 (2004).

[27] M. Kimura and H. Horiuchi, Nucl. Phys. **A767**, 58 (2006).